Angular momentum invoked band inversions in mirror symmetry protected topological states

Dexin Li,[1] Mingxiang Pan,[1] Citian Wang,[1] and Huaqing Huang[1,2,3,*]
[1]*School of Physics, Peking University, Beijing 100871, China*
[2]*Collaborative Innovation Center of Quantum Matter, Beijing 100084, China*
[3]*Center for High Energy Physics, Peking University, Beijing 100871, China*

(Received 7 March 2022; accepted 11 May 2022; published 23 May 2022)

The notion of a band inversion provides an intuitive physical paradigm for understanding the electronic band topology. Here we study the general band inversion mechanism, which exploits local atomic orbitals and lattice symmetry, in mirror protected topological crystalline insulators (TCIs). Based on low-energy effective theory analysis, we find that for these mirror protected TCIs, the topological invariant (i.e., the mirror Chern number $\mathcal{C}_M$) is determined by the difference of total magnetic quantum numbers m_j of orbitals involved in the band inversion: $|\mathcal{C}_M| = |\Delta m_j|$. This angular-momentum criterion is further verified by the atomic tight-binding model calculations in two-dimensional (2D) crystalline, quasicrystalline, and disordered lattices. Moreover, such an angular momentum invoked band inversion (AMBI) is also extendable to 3D lattices and gives rise to topological semimetals with Dirac points in the bulk and double Fermi arcs on surfaces. As a concrete material example, we further predict that the Ba monolayer is an AMBI-induced TCI by first-principles calculations. In addition, we also show that a large number of previously proposed TCI materials satisfy the AMBI mechanism. Our findings not only provide an alternative understanding of mirror protected band topology but also offer useful guidance for designing or engineering mirror protected TCI materials.

DOI: 10.1103/PhysRevB.105.195133

I. INTRODUCTION

Topological states of matter are among the most intriguing research topics of condensed matter physics during the past decade [1–3]. Topological states usually differ from conventional ones in that they are characterized by a nontrivial bulk topological invariant associated with certain symmetry class and manifest special topological edge or surface states due to the bulk-boundary correspondence [4,5]. For example, topological insulators (TIs), which are topologically protected by time-reversal symmetry, are classified by a binary-valued $\mathbb{Z}_2$ topological invariant and manifest as insulting in the bulk and conductive on the boundary [6,7]. So far, TIs have been theoretically predicted and experimentally verified in various 2D materials, such as HgTe/CdTe quantum wells [8], and 3D compounds like the Bi_2Se_3 family of materials [9]. In addition to time-reversal symmetry protected TIs, topological states can also arise from generic crystalline symmetries, which give rise to the so-called topological crystalline insulators (TCIs) [10,11]. Although many TCI phases depending on different crystal symmetries have been proposed [12–18], yet those relying on mirror symmetry [19] are of particular interest, as they have been experimentally observed in IV-VI semiconductors, such as SnTe material class [20–24], and theoretically predicted in various 2D and 3D systems [25–39]. These TCIs, which are characterized by a mirror-related topological invariant, namely, the mirror Chern number $\mathcal{C}_M$ [40], manifest also with topological boundary states but only at those surfaces/edges that preserve the underlying mirror symmetry.

An intuitive physical picture to understand topological states is that the nontrivial band topology usually involves an inverted band order between occupied and unoccupied Bloch states at high-symmetry **k** points of the Brillouin zone (BZ) [41–43]. Such band inversion usually marks the transition from normal states to some kinds of topological states. In general, the type of band inversion can be indicated by the eigenvalues of spatial symmetry operators of inverted bands. For example, according to the Fu-Kane parity criterion for nonmagnetic materials with inversion symmetry [44], the $\mathbb{Z}_2$ indices are determined by simple combinations of the parities (i.e., inversion eigenvalues) of the occupied bands at time-reversal invariant momentum. Therefore band inversions between states with opposite parity around the Fermi level play a key role in the realization of the quantum spin Hall (QSH) effect and 3D topological insulators [8,45].

In practical material calculations based on the density functional theory or tight-binding models, band inversions are usually characterized by an exchange of orbital components between conduction and valence bands around the high-symmetry **k** point, and sometimes exhibit an M-shape or W-shape band dispersion in the vicinity of that point [46]. These typical features of band inversions not only provide significant hints for computational seeking topological materials (even for systems without inversion symmetry), but also offer a useful guidance for engineering topological phase transitions by chemical doping, strain, or external fields [47–49]. Recently, a comprehensive theory of symmetry-based indicator [50–52] has been established to diagnose underlying

*Corresponding author: huaqing.huang@pku.edu.cn

band topology of crystalline materials. Consequently, band inversions characterized by different crystalline symmetry eigenvalues imply the existence of different types of TCI phases [12,53]. In this work, we study this type of band inversion, with a particular focus on the orbital symmetry which directly relates to its orbital angular momentum. Such a band inversion is expected to signal TCI phases in both crystalline and noncrystalline systems as long as the essential symmetry under concern is preserved.

Specifically, we provide a generic approach to analyze mirror protected TCIs from the perspective of band inversion invoking the angular momentum of the inverted states, which dubbed angular momentum invoked band inversions (AMBIs). We derive a generic low-energy effective theory of AMBI and prove that the mirror Chern numbers of the TCIs induced by AMBIs are determined by the difference of total magnetic quantum number m_j of the inverted states: $|\mathcal{C}_M| = |\Delta m_j|$. Such AMBI-induced TCIs and the angular-momentum criterion of $\mathcal{C}_M$ are numerically demonstrated in both 2D crystals and structurally disordered lattices preserving the mirror plane. We further extend the AMBI mechanism to 3D and find that topological Dirac semimetals can be induced by AMBIs. Finally, we discuss material implementations of TCIs that exhibit AMBIs, validating our proposed formula in realistic materials that are experimentally accessible.

II. ANGULAR-MOMENTUM INVOKED BAND INVERSION

We particularly focus on 2D planar systems with the time-reversal symmetry T and the in-plane mirror symmetry M_z: $z \to -z$. Mirror protected TCIs are identified by a nonzero mirror Chern number $\mathcal{C}_M$, which is defined as the half difference between the Chern number for the two mirror subspace: $\mathcal{C}_M = (\mathcal{C}_+ - \mathcal{C}_-)/2$. To determine $\mathcal{C}_M$, we should first divide occupied Bloch states into two mirror subspaces and then calculate the Chern number for each subspace separately. Since the mirror operation can be expressed as the combination of inversion I and twofold rotation C_{2z}, the representation of the mirror operator under the orbital basis $|l, m_l\rangle$ and spin basis $|s = \frac{1}{2}, m_s = \pm\frac{1}{2}\rangle$ (i.e., spin up and down states $|\uparrow\ \downarrow\rangle$) are

$$\hat{M}_z^{\text{orb}} = (-1)^l e^{-\frac{i}{\hbar}\hat{L}_z\pi} = (-1)^{l+m_l}, \tag{1}$$

$$\hat{M}_z^{\text{spin}} = e^{-\frac{i}{\hbar}\hat{S}_z\pi} = -\frac{2i}{\hbar}\hat{S}_z = -i\tau_z, \tag{2}$$

where $\hat{L}_z$ ($\hat{S}_z$) is the z component of orbital (spin) angular momentum operators $\mathbf{L}$ ($\mathbf{S}$), τ_z is the third Pauli matrix for spin degree of freedom, and $i = \sqrt{-1}$. Consequently, the mirror operator under $|LS\rangle = |l, m_l\rangle \otimes |s, m_s\rangle$ is

$$\hat{M}_z = \hat{M}_z^{\text{orb}}\hat{M}_z^{\text{spin}} = -i(-1)^{l+m_l}\tau_z. \tag{3}$$

Noting that the mirror eigenvalue of state $|l, m_l\rangle$ is determined by the modulo-2 value of $(l + m_l)$, we thus divide atomic orbitals into two classes accordingly. As shown in Fig. 1, orbitals with even (odd) l are inversion I-symmetric (antisymmetric), and orbitals are M_z-symmetric (antisymmetric) if their $(l + m_l)$ are even (odd). For convenience, we divide our discussion of band inversions into two types: orbitals with the same (type-I) or opposite mirror eigenvalues (type-II).

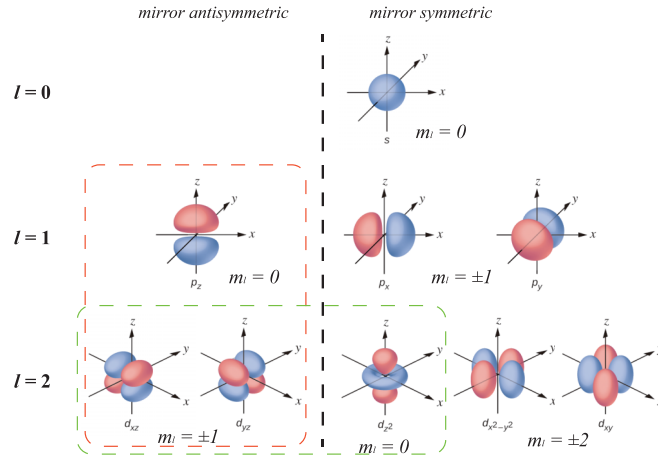

FIG. 1. Atomic orbitals with different angular momentum l and magnetic quantum number m_l are divided into two groups according to their eigenvalues of in-plane mirror operator $\hat{M}_z$. Orbitals in the red (green) dashed-line box are used to illustrate the mirror protected TCI with $|\mathcal{C}_M| = 1$ ($|\mathcal{C}_M| = 2$) which are induced by type-I (type-II) AMBI between orbitals with the same (opposite) mirror eigenvalues.

We start by introducing the general band inversion from a low-energy perspective. Without loss of generality, let's consider a band inversion between conduction and valence bands at the Γ point (i.e., $\mathbf{k} = 0$). A four-band low-energy model (including spin degree of freedom) is sufficient to consider the band inversion for orbitals with different angular momentum. Firstly, we consider the type-I band inversions that involve orbitals with the same mirror eigenvalues. The mirror operator $\hat{M}_z$ under these bases is equivalent to the spin operator $\hat{S}_z$ up to an inessential factor, indicating that $\mathcal{C}_M$ is equal to the spin Chern number $\mathcal{C}_s = (\mathcal{C}_\uparrow - \mathcal{C}_\downarrow)/2$, which is defined as the half difference between the Chern numbers for the two spin subspaces of the occupied bands [54–56]. As the division of mirror subspace is consistent with spin subspace, the effective Hamiltonian is block-diagonal for mirror and spin subspace simultaneously,

$$H(\mathbf{k}) = \begin{pmatrix} h(\mathbf{k}) & 0 \\ 0 & h^*(-\mathbf{k}) \end{pmatrix}, \tag{4}$$

$$h(\mathbf{k}) = \epsilon(\mathbf{k})I_{2\times 2} + \mathbf{d}(\mathbf{k}) \cdot \boldsymbol{\sigma}, \tag{5}$$

where $I_{2\times 2}$ is a 2×2 identity matrix and $\boldsymbol{\sigma} = (\sigma_x, \sigma_x, \sigma_x)$ are the Pauli matrices for orbital degree of freedom. Here $h(\mathbf{k})$ is the two-band Hamiltonian in the subspace with certain spin and mirror eigenvalues. Since the overall dispersion term $\epsilon(\mathbf{k})$ doesn't affect the topological invariant, we neglect it hereafter, unless otherwise specified. In the spin up subspace, for a band inversion between orbitals $|l_1, m_{l,1}\rangle \otimes |\uparrow\rangle$ and $|l_2, m_{l,2}\rangle \otimes |\uparrow\rangle$, we can expand $h(\mathbf{k})$ to the leading order of $\mathbf{k}$ near the Γ point,

$$h_{\text{eff}}(\mathbf{k}) = \mathbf{d}(\mathbf{k}) \cdot \boldsymbol{\sigma} = \varepsilon\sigma_z + \delta(k_+^{\Delta m_l}\sigma_- + k_-^{\Delta m_l}\sigma_+), \tag{6}$$

where ε and δ are the energy difference and coupling strength of the two bands, $k_\pm = k_x \pm ik_y$ and $\sigma_\pm = (\sigma_x \pm i\sigma_y)/2$. $\Delta m_l = m_{l,1} - m_{l,2}$ is the difference of the orbital magnetic quantum number. The Chern number of the two-band subspace Hamiltonian (6) is given by $|\mathcal{C}| = |\frac{1}{4\pi}\int d^2\mathbf{k}(\partial_{k_x}\hat{d} \times \partial_{k_y}\hat{d}) \cdot \hat{d}| = |\Delta m_l|$, where $\hat{d} = \mathbf{d}(\mathbf{k})/|\mathbf{d}(\mathbf{k})|$. Since the two

blocks in Eq. (4) are connected by time-reversal symmetry T, the opposite mirror/spin subspace is spanned by the basis of $|l_1, -m_{l,1}\rangle \otimes |\downarrow\rangle$ and $|l_2, -m_{l,2}\rangle \otimes |\downarrow\rangle$ and $h^*(-\mathbf{k})$ has an opposite Chern number. Due to the equivalence between $\hat{M}_z$ ($\sim\sigma_0\tau_z$) and $\hat{S}_z$ ($\sim\tau_z$), we find that the difference in m_l is the same as that in m_j, i.e., $\Delta m_l = \Delta m_j$. Here m_j is the magnetic quantum number for the z component $\hat{J}_z$ of total angular momentum $\mathbf{J}$. Finally, the topological invariant of the total Hamiltonian is

$$|\mathcal{C}_M| = |\mathcal{C}_s| = |\Delta m_l| = |\Delta m_j|. \tag{7}$$

Given the fact that the spin Chern number $\mathcal{C}_s$ can also formulate the $\mathbb{Z}_2$ classification of TIs via $\mathbb{Z}_2 = (\mathcal{C}_s \mod 2)$, Eq. (7) implies that a TCI with an odd-number $\mathcal{C}_M$ in this case is also a TI protected by time-reversal symmetry T. Therefore topological edge states of a TCI with an odd-number $\mathcal{C}_M$ are robust against nonmagnetic perturbations that break the mirror symmetry, as long as the energy gap does not close.

Secondly, we consider the type-II band inversions between orbitals with opposite mirror eigenvalues. The mirror subspace composed of states with opposite spins is no longer consistent with the spin subspace. To achieve nonzero Chern numbers within a mirror subspace (and thus lead to TCIs with nonzero $\mathcal{C}_M$), spin mixing terms, such as spin-orbit coupling (SOC), are required in the Hamiltonian. Because the intrinsic SOC operator, which is expressed as $\mathbf{L}\cdot\mathbf{S} = \hat{L}_z\hat{S}_z + (\hat{L}_-\hat{S}_+ + \hat{L}_+\hat{S}_-)/2$, does not vanish only between orbitals with $\Delta l = 0$ and $|\Delta m_l| = 1$. We, therefore, just need to consider band inversions in this situation.

Without loss of generality, we choose $|m_{l,1} = \pm m_1\rangle$ and $|m_{l,2} = \pm(m_1+1)\rangle$ which have opposite mirror eigenvalues as basis ($m_1 \geqslant 0$), and the effective Hamiltonian shares a similar block-diagonal form as Eq. (4), except that $h(\mathbf{k})$ is now a four-band mirror-polarized subspace Hamiltonian under the basis of $|\pm m_1\rangle \otimes |\uparrow\rangle$ and $|\pm(m_1+1)\rangle \otimes |\downarrow\rangle$. For convenience, we rearrange the basis to the $|m_l, m_j\rangle$ representation with the conservation of total angular momentum, which reads

$$\left.\begin{matrix} |\pm m_1\rangle \otimes |\uparrow\rangle \\ |\pm(m_1+1)\rangle \otimes |\downarrow\rangle \end{matrix}\right\} \Rightarrow \begin{cases} |m_1, m_1+\frac{1}{2}\rangle \\ |m_1, -m_1+\frac{1}{2}\rangle \\ |m_1+1, -m_1-\frac{3}{2}\rangle \\ |m_1+1, m_1+\frac{1}{2}\rangle \end{cases}. \tag{8}$$

There are only two possible AMBIs that lead to the nontrivial topology. One is between $|m_1+1, m_1+\frac{1}{2}\rangle$ and $|m_1, -m_1+\frac{1}{2}\rangle$. We project the subspace Hamiltonian $h(\mathbf{k})$ to the two states, which yields

$$h_{\text{eff}}(\mathbf{k}) = \varepsilon\sigma_z + \lambda\delta(k_+^{\Delta m_j}\sigma_- + k_-^{\Delta m_j}\sigma_+), \tag{9}$$

where $\Delta m_j = (m_1+1/2) - (-m_1+1/2) = 2m_1$ and λ represent the strength of SOC. Equation (9) is pedagogically derived in Appendix. Accordingly, the band inversion induced Chern number in the mirror subspace is $|\mathcal{C}| = \Delta m_j$, and the mirror Chern number of the full Hamiltonian is $|\mathcal{C}_M| = \Delta m_j$. Similarly, for the other possible band inversion between $|m_1, m_1+\frac{1}{2}\rangle$ and $|m_1+1, -m_1-\frac{3}{2}\rangle$, we also arrive at $|\mathcal{C}_M| = \Delta m_j = (m_1+\frac{1}{2}) - (-m_1-\frac{3}{2}) = 2m_1+2$. As an example, let's consider the special case of $m_1 = 0$, the only nontrivial band inversion occurs between $|0, \pm\frac{1}{2}\rangle$ and $|1, \mp\frac{3}{2}\rangle$ which leads to a TCI with $|\mathcal{C}_M| = 2$.

TABLE I. Possible orbital combinations for AMBIs.

type	$(\Delta l, \lvert\Delta m_l\rvert)$	atomic orbitals	$\lvert\mathcal{C}_M\rvert$
I	(1,1)	s vs $p_x + p_y$	1
		p_z vs $d_{xz} + d_{yz}$	
		d_{z^2} vs $p_x + p_y$	
		$p_x + p_y$ vs $d_{x^2-y^2} + d_{xy}$	1,3
	(2,2)	s vs $d_{x^2-y^2} + d_{xy}$	2
	(0,2)	d_{z^2} vs $d_{x^2-y^2} + d_{xy}$	
II	(0,1)	p_z vs $p_x + p_y$	2
		d_{z^2} vs $d_{xz} + d_{yz}$	
		$d_{xz} + d_{yz}$ vs $d_{x^2-y^2} + d_{xy}$	2,4

The above analysis demonstrates that for both type-I and type-II AMBIs, the mirror Chern number $\mathcal{C}_M$ of AMBI-induced TCIs is simply determined by the difference of total magnetic quantum number m_j between states involved in the band inversion:

$$|\mathcal{C}_M| = |\Delta m_j|. \tag{10}$$

Therefore one can extract the topological invariant of a material by performing orbital analysis for its electronic band structures. Table I lists all possible combinations of orbitals for nontrivial AMBIs.

Despite a similar dependence of the mirror Chern number $\mathcal{C}_M$ on angular momenta of inverted orbitals, there are still significant differences between the type-I and type-II AMBIs. The spin conservation symmetry and mirror symmetry play the same role in the type-I AMBI, revealing the close link between the QSH state and the aforementioned type-I AMBI-induced TCI state. Therefore, even if the mirror symmetry is broken, the type-I AMBI mechanism can still be applicable to signal nontrivial $\mathbb{Z}_2$ topology. However, when there is a certain spin-mixing effect between the inverted orbitals, the type-II AMBI is supposed to be considered and the mirror symmetry is indispensable to protect the topology.

Before proceeding, we have a few remarks. First, the analysis can be directly generalized to 3D with mirror symmetry, where topological surface states appear at surfaces preserving the essential mirror symmetry. Secondly, it is straightforward to generalize to systems with multiple AMBIs at the same or different $\mathbf{k}$ points of the BZ, and the total mirror Chern number is just the contribution of all AMBIs. In addition to the mirror symmetry M_z, other lattice symmetries which may lead to extra constraints to the low-energy Hamiltonian, are not considered in the above analysis. Therefore, for crystals with different spatial symmetries, AMBI may also induce topological semimetals with nodal points or lines that are protected by other lattice symmetries. Moreover, noting that the topological property will not change as long as the energy gap does not close during any adiabatic process, we expect that the AMBI-induced TCI can also persist in certain noncrystalline systems with mirror symmetry. Finally, although the above analysis is based on the single-electron picture, it can straightforwardly generalize to TCIs with strong electron interactions. When the effect of electron interactions is considered, the original

integer $\mathbb{Z}$ classification of noninteracting TCIs (indexed by the mirror Chern number $\mathcal{C}_M$), is reduced to $\mathbb{Z}_4$ in 2D and $\mathbb{Z}_8$ in 3D [57,58]. Therefore the topological invariant of interacting TCIs in 2D and 3D are $\mathcal{C}_M$ modulo 4 and 8, respectively.

III. METHOD

To numerically study the effect of AMBIs on the band topology, we consider a general tight-binding Hamiltonian

$$H = \sum_{i\mu s} \epsilon_i^{\mu s} c_{i\mu s}^\dagger c_{i\mu s} + \sum_{\langle ij\rangle} \sum_{\mu\nu,s} t_{\mu\nu}(\mathbf{r}_{ij}) c_{i\mu s}^\dagger c_{j\nu s} + \sum_i \sum_{\mu\nu} \sum_{ss'} \lambda_i^{\mu\nu} \langle \mu s|\mathbf{L}\cdot\mathbf{S}|\nu s'\rangle c_{i\mu s}^\dagger c_{i\nu s'}, \quad (11)$$

where $c_{i\mu s}^\dagger (c_{i\mu s})$ is electron creation (annihilation) operator on the μ orbital with spin $s(=\uparrow\downarrow)$ at the ith site. $\epsilon_i^{\mu s}$ is the on-site energy and $t_{\mu\nu}(\mathbf{r}_{ij})$ is the Slater-Koster hopping integral which depends on orbital types and the intersite vector $\mathbf{r}_{ij}$ [59]. $\mathbf{L}$ and $\mathbf{S}$ are the orbital and spin angular momentum operators, respectively. $\lambda_i^{\mu\nu}$ is the SOC strength [60].

As a concrete material example, we study the electronic structure and band topology of the Ba monolayer. We carry out first-principles calculations within the framework of density functional theory as implemented in the Vienna *ab initio* simulation package [61]. The projector augmented-wave method [62] and the Perdew-Burke-Ernzerhof-type exchange-correlation functional [63] are used in our calculations. The plane-wave energy cutoff is set to 600 eV, and the BZ is sampled by a Monkhorst-Pack $\mathbf{k}$-point mesh of $8\times8\times1$. The topological properties are calculated using a tight-binding Hamiltonian based on Wannier functions [64,65], which are constructed by projecting bulk Bloch wave functions into s, p and d orbitals of Ba.

To obtain the mirror Chern number, we divide the occupied states in the mirror-invariant plane of the BZ into two separate sets according to their mirror eigenvalues and calculate their respective Chern numbers. Numerically, the Chern number is calculated using a gauge-invariant formula

$$\mathcal{C} = \frac{1}{2\pi} \sum_{\mathbf{k}\in \mathrm{BZ}} \mathrm{Tr}[\mathcal{F}_{mn}(\mathbf{k})], \quad (12)$$

where $\mathcal{F}_{mn}(\mathbf{k}) = -2\mathrm{Im}\langle\partial_{k_x} u_m(\mathbf{k})|\partial_{k_y} u_n(\mathbf{k})\rangle$ is the non-Abelian Berry curvature defined in the discretized BZ [66], $|u_n(\mathbf{k})\rangle$ is the cell-periodic part of the Bloch wave function of the nth occupied band, and Tr denotes a trace over all occupied bands.

Alternatively, one can also determine the Chern number by tracing the evolution of the Wannier charge center (WCC) using the Wilson loop method. A Wilson loop is an arbitrary closed $\mathbf{k}$-point loop in the BZ, evaluated around which the occupied Bloch functions acquire a total Berry phase $\theta(w)$, with w being the loop index. One can define a series of parallel Wilson loops w to fully cover the 2D BZ. Then, the evolution of $\theta(w)$ along these parallel Wilson loops gives information on the band-structure topology on the 2D BZ [67,68]. For a 2D crystal, we define Wilson loops along the k_x direction with fixed k_y,

$$D(k_y) = \mathcal{P}\exp\left(-i\int_{C_{k_y}} \mathcal{A}(\mathbf{k})dk_x\right), \quad (13)$$

where C_{k_y} is a contour with fixed k_y which goes across the BZ in k_x, $\mathcal{A}(\mathbf{k})$ is the Berry connection of occupied bands and $\mathcal{P}$ is the path-ordering operator. The WCCs are identified as the phases $\theta_m(k_y)\in[0,2\pi)$ of the mth eigenvalues $\lambda_m(k_y)$ of $D(k_y)$, i.e., $\theta_m(k_y) = -\mathrm{Im}\ln\lambda_m(k_y)$. Within the periodic evolution of k_y, the sum of WCCs will wind $[0,2\pi)$ an integer times, which gives the Chern number.

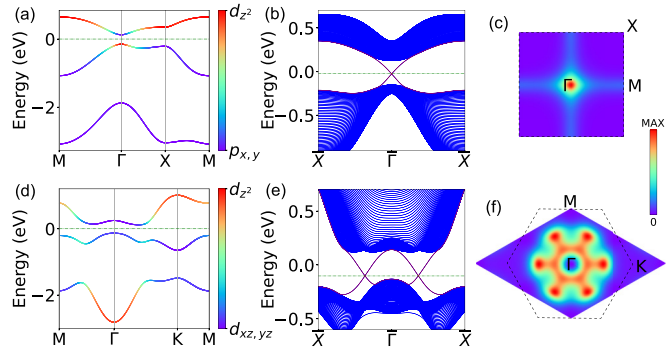

FIG. 2. [(a)–(c)] TCI with $\mathcal{C}_M = 1$ in a square lattice due to an AMBI between d_{z^2} and (p_x, p_y) orbitals. [(d)–(f)] TCI with $\mathcal{C}_M = -2$ in a triangular lattice due to an AMBI between d_{z^2} and (d_{xz}, d_{yz}) orbitals. The parameters used in (a)–(c) are $\epsilon_{d_{z^2}} = 0.3$, $\epsilon_{p_x,p_y} = -1.55$, $V_{pp\sigma} = 0.4$, $V_{pp\pi} = -0.1$, $V_{pd\sigma} = -0.4$, $V_{pd\pi} = 0.1$, $V_{dd\sigma} = -0.1$, $V_{dd\pi} = 0.1$, $V_{dd\delta} = -0.1$, and $\lambda = 1$ eV. The parameters used in (d)–(f) are $\epsilon_{d_{z^2}} = -0.35$, $\epsilon_{d_{xz},d_{yz}} = -0.65$, $V_{dd\sigma} = -1.2$, $V_{dd\pi} = 0.3$, $V_{dd\delta} = -0.1$, and $\lambda = 0.3$ eV. [(a) and (d)] Orbital-resolved bulk band structures. [(b) and (e)] Edge spectrum of ribbon structures where the topological edge states are marked in red. [(c) and (f)] Mirror-graded Berry curvatures associated with $+i$ $(-i)$ mirror eigenstates in the first BZ of the square (triangular) lattice, respectively.

IV. RESULTS

A. AMBI-induced TCI in 2D periodic lattices

We first consider an atomic-basis model with a type-I AMBI between d_{z^2} $(l=2, m_l=0)$ and degenerate $p_{x,y}$ $(l=1, m_l=\pm1)$ orbitals in a square lattice. Since all these orbitals are M_z-symmetric, the mirror Chern number should be $|\mathcal{C}_M| = |\Delta m_l| = 1$, according to Eq. (7). As shown in Fig. 2, the orbital-resolved band structure exhibits a clean signature of d-p band inversion around the Γ point, indicating its nontrivial topology. To identify the TCI state, we calculate the mirror Chern number by integrating mirror-graded Berry curvature associated with positive/negative mirror eigenstates over the 2D BZ [see Fig. 2(c)] and find $\mathcal{C}_M = 1$, which is consistent with the above analysis of AMBI. Due to the bulk-edge correspondence, the nonzero mirror Chern number also guarantees the existence of topological edge states in the bulk gap, as displayed in Fig. 2(b).

Next, we construct another model in a triangular lattice to realize a type-II AMBI between d_{z^2} $(l=2, m_l=0)$ and degenerate $d_{xz,yz}$ $(l=2, m_l=\pm1)$ orbitals, which have

opposite mirror eigenvalues. Such a subgroup of d orbitals can be separated from the rest by crystal field splitting [69]. The AMBI would induce a TCI with the mirror Chern number $|\mathcal{C}_M| = |\Delta m_j| = 2$. Our numerical calculations show that the d-d band inversion in the bulk bands [see Fig. 2(d)] gives rise to the mirror Chern number of $\mathcal{C}_M = -2$, confirming our derived criterion in Eq. (10). As shown in Fig. 2(d), the existence of two pairs of topological edge states is also consistent with the calculated mirror Chern number, lending additional support to our identification of the AMBI-induced TCI state.

To validate the generality of AMBI, we systemically carry out the tight-binding calculations for all possible combinations of orbitals listed in Table I. With properly selected parameters, a total of 11 kinds of AMBIs can be realized and the obtained mirror Chern numbers agree with the above analysis from the total angular momentum of the states involved in the band inversion. As the underlying physics of our proposed TCIs are dominated by AMBI at the Γ point, the topological nature should be robust against any mirror symmetry-preserved perturbations as long as the bulk gap does not close. Therefore it is expected that the AMBI-induced TCIs are also applicable to various crystalline lattices and certain noncrystalline lattices with the essential mirror symmetry. To verify this hypothesis, we consider the AMBI in two kinds of noncrystalline lattices without translational symmetry, quasicrystals and amorphous lattices.

B. AMBI-induced TCI in 2D quasicrystals and amorphous lattices

We construct the quasicrystalline lattices based on the rhombic Penrose tiling which have fivefold rotational symmetry but lack translational symmetry [70–73]. Based on a similar tight-binding model used in Figs. 2(a)–2(c), we can realize an AMBI between d_{z^2} and $p_{x,y}$ in the quasicrystalline lattice. We first estimate the bulk energy gap of the Penrose-tiling quasicrystal by calculating a series of quasicrystal approximants which are periodic approximations of the quasicrystal [74–76]. We then calculate the energy spectrum of a finite pentagonal sample of the Penrose-tiling quasicrystal, as shown in Fig. 3(a). Remarkably, the energy spectrum of a finite sample is quasicontinuous in the bulk gap region. The states residing inside the bulk gap are localized on the boundary of the finite quasicrystal sample. As an example, we plot the spatial distribution of a typical in-gap state in Fig. 3(b). We also study other finite quasicrystal samples with different boundary geometries, and find that the edge states robustly remain on the boundary regardless of their detailed shapes. This implies that the system should be a topologically nontrivial state. To verify that the system is an AMBI-induced TCI, we further calculate the real-space topological invariant, the mirror Bott index $\mathcal{B}_m$, which enables the identification of the mirror Chern number in noncrystalline systems [77]. The calculated $\mathcal{B}_m = 1$ for the quasicrystalline system in Figs. 3(a) and 3(b), confirms the AMBI-induced TCI in the quasicrystal. For comparison, we also examine the topologically trivial state in quasicrystal by tuning the parameter $\epsilon_{d_{z^2}}$ to 2.1 eV, which drives the quasicrystal into a trivial state with $\mathcal{B}_m = 0$. It is found that the in-gap edge states vanish in the trivial quasicrystal, confirming the topological origin of the in-gap edge states of the above Penrose-tiling quasicrystal with an AMBI.

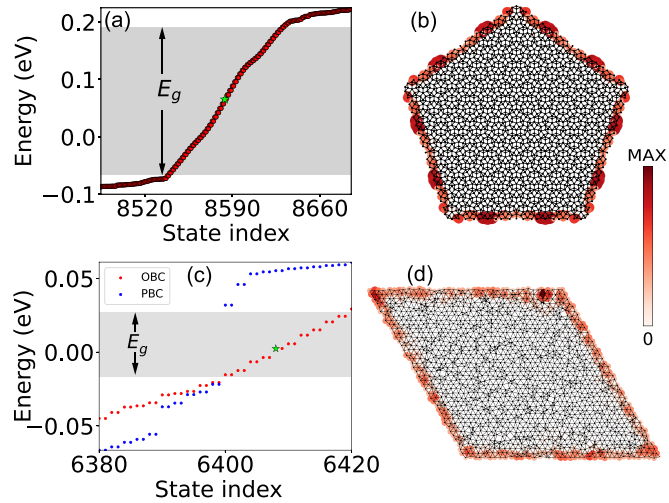

FIG. 3. [(a) and (b)] TCI in a Penrose-tiling quasicrystal with 2146 sites due to an AMBI between d_{z^2} and (p_x, p_y) orbitals and [(c) and (d)] TCI in an amorphous system due to an AMBI between d_{z^2} and (d_{xz}, d_{yz}) orbitals. The amorphous system is constructed from a 40×40 supercell of the triangular lattice by introducing random atomic displacement away from its equilibrium position for each atom. The parameters used in (a) and (b) are $\epsilon_{d_{z^2}} = 0.7$, $\epsilon_{p_x,p_y} = -2.3$, $V_{pp\sigma} = 0.34$, $V_{pp\pi} = 0.34$, $V_{pd\sigma} = -0.34$, $V_{dd\sigma} = -0.44$, $V_{dd\delta} = -0.08$, and $\lambda = 1.0$ eV. The parameters used in (c) and (d) are $\epsilon_{d_{z^2}} = -0.35$, $\epsilon_{d_{xz},d_{yz}} = -0.65$, $V_{dd\sigma} = -1.2$, $V_{dd\pi} = 0.3$, $V_{dd\delta} = -0.1$, and $\lambda = 0.3$ eV. [(a) and (c)] Energy levels near the Fermi level. The eigenvalues with PBC and those with OBC are marked in blue and red, respectively. [(b) and (d)] The real-space distribution of one of the in-gap edge states [marked as green star in (a) and (c)].

After that, we investigate the effect of the in-plane structural amorphization which breaks translational symmetry of the 2D lattice [78–80]. As an illustrative example, we start from a 40×40 supercell of the perfect 2D triangular lattice studied in Figs. 3(d)–3(f) and assign random atomic displacement $\boldsymbol{\delta} = (d\cos\theta, d\sin\theta)$ away from its equilibrium position for each atom, where θ is a random azimuth angle uniformly distributed in the interval $[0, 2\pi)$. The amplitude d of atomic displacements are uniformly distributed in the range $[0, 0.3a)$ with a being the lattice constant. As shown in Fig. 3(c), the disordered system with a periodic boundary condition (PBC) shows an energy gap, indicating that it is still an insulator. However, a set of states appears in the gap region when an open boundary condition (OBC) is applied, implying that the system with edges becomes metallic. The spatial distribution of these in-gap states in Fig. 3(d) confirms that they are localized edge states. We further identify the TCI state by calculating the mirror Bott index $\mathcal{B}_m$. For the disordered system in Figs. 3(c) and 3(d), we find that the mirror Bott index $\mathcal{B}_m = -2$, indicating that it is indeed a TCI.

C. AMBI-induced topological semimetals in 3D

Given the vase interest enjoyed by the three-dimensional topological crystalline insulators such as SnTe, we also

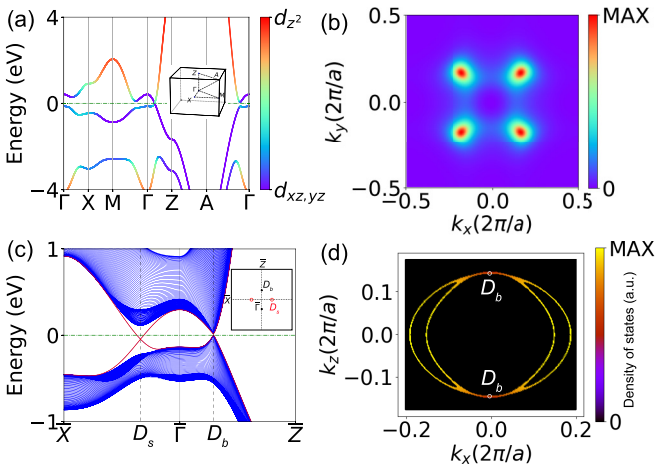

FIG. 4. Topological Dirac semimetal in the 3D simple cubic lattice due to AMBI between d_{z^2} and $d_{xz,yz}$. The parameters used here are $\epsilon_{d_{z^2}} = 4.2$, $\epsilon_{d_{xz,yz}} = -2.8$, $V_{dd\sigma} = -2.4$, $V_{dd\pi} = 0.9$, $V_{dd\delta} = -0.2$, and $\lambda = 0.6$ eV. (a) The calculated bulk band structure of the cubic lattice. The inset shows the first BZ with high-symmetry **k** points. (b) The distribution of $-i$ mirror-graded Berry curvature in the $k_z = 0$ plane of the first BZ. (c) Surface band structure of the (010) surface where the surface states are marked in red. The inset shows the surface BZ with the projection of the bulk Dirac points (D_b) and surface Dirac points (D_s). (d) Fermi Surface of the (010) surface where double Fermi arcs connecting two projected bulk Dirac points (D_b).

investigate the possibility of generalizing the AMBI mechanism to 3D. As an example, we consider a model in the simple cubic lattice with an AMBI between d_{z^2} and degenerate $d_{xz,yz}$ orbitals. As shown in Fig. 4(c), although there is an AMBI around the Γ point, the band orders are not inverted at other high-symmetry **k** points of the BZ. Remarkably, the conduction and valence bands cross along the Γ-Z line, forming a Dirac point. This is because of the high symmetry of the cubic lattice. As two bands along this line belong to different irreducible representations of the space group, they can cross each other without opening a gap. The existence of gapless Dirac points indicates that the system becomes a topological Dirac semimetal [81–84]. To reveal its topological nature, we calculate the mirror-graded Berry curvature and mirror Chern number in both the $k_z = 0$ and $k_z = \pi$ planes where the band structures are fully gapped. As shown in Fig. 4(b), the mirror-graded Berry curvature is strongly concentrated in the vicinity of the Γ point in the $k_z = 0$ plane, which justifies our analysis of band inversions from orbital components of bands. However, there is no significant distribution of Berry curvature in the $k_z = \pi$ plane. We calculate the mirror Chern numbers by numerically integrating the mirror-graded Berry curvature for all occupied bands over the entire 2D BZ with fixed k_z, and find that $\mathcal{C}_M = -2$ and 0 for the $k_z = 0$ and $k_z = \pi$ planes, respectively.

One of the most important consequences of Dirac semimetal is the existence of topological surface states and Fermi arcs on the surface [47,48]. Due to the nonzero mirror Chern number, the 3D Dirac semimetal supports 2D surface Dirac cones when a surface parallel to the k_z axis is introduced, and the number of 2D Dirac cones on one surface is given by $|\mathcal{C}_M| = 2$. We calculate the (010) surface states of the cubic lattice, as shown in Figs. 4(c) and 4(d). As expected, two 2D surface Dirac cones appear on the k_x axis and are symmetrical about the Γ point [one of them is shown in Fig. 4(c)]. As shown in Fig. 4(d), the Fermi surface of the (010) surface is composed of four pieces of Fermi arcs, which connect the two projections of bulk Dirac points. As the number of surface Dirac cones is two, the number of surface Fermi arcs is also doubled as compared with conventional Dirac semimetals with only two pieces of Fermi arcs. It is worth noting that the number of the Fermi arcs on the surface of the 3D Dirac semimetal is solely determined by the mirror Chern number on the $k_z = 0$ (or $k_z = \pi$) plane irrespective of the energy dispersion around the 3D Dirac point. This is clearly distinct from Weyl semimetals where the number of Fermi arcs is determined by local dispersion around the Weyl point (which determines the topological charge) and the number of Weyl point pairs in the first BZ [85]. Therefore Dirac semimetals with different numbers of Fermi arcs can be realized by different kinds of AMBIs.

The existence of Fermi arcs, which stem from the bulk 3D Dirac points, identifies the nontrivial topological nature of the AMBI-induced Dirac semimetal. In addition to the 3D topological Dirac semimetal studied here, it is also possible to obtain a 3D TCI or weak TI, as both the $k_z = 0$ and $k_z = \pi$ planes can have nonzero mirror Chern numbers of $|\mathcal{C}_M| = 1$ or 2 when AMBIs occur at both planes.

D. Material example: Ba monolayer

Finally, we study the Ba monolayer as a concrete material example of AMBI-induced TCIs. Although previous works show that both the pure alkali earth metal of Ba and barium compounds (e.g., stannides, germanides, and silicides) are topological nodal line semimetals with nontrivial drumhead surface states [86–88], the 2D monolayer of Ba has not been studied yet. Here we perform the first-principles calculations for the Ba monolayer in square planar lattice with an optimized lattice constant $a = 4.5$ Å. As shown in Fig. 5(a), the conduction and valence bands near the Fermi level almost cross with each other along the M-X line with a small energy gap of $E_g = 30$ meV. Moreover, the irrelevant conduction band near the gap can be pushed up by a tensile strain which can be introduced by the epitaxial growth on substrates with lattice mismatch. Remarkably, the orbital-contribution analysis shows that the bulk bands show an AMBI around the M point between states dominated by (s, d_{z^2}) and $(d_{x^2-y^2}, d_{xy})$, implying the nontrivial band topology. As listed in Table I, such AMBI leads to a nonzero mirror Chern number of $|\mathcal{C}_M| = 2$.

To determine the mirror Chern number, we then apply the Wilson loop method to calculate the evolution of the WCCs of occupied bands with opposite mirror eigenvalues. Specifically, we define Wilson loops along the k_x direction with fixed k_y. All the occupied bands at **k** points in the 2D BZ are classified into two groups according to their mirror eigenvalues. Taking those that have $\pm i$ mirror eigenvalues, the evolution of Berry phases along the periodic k_y direction can be obtained as the mirror-graded WCC, and the mirror Chern

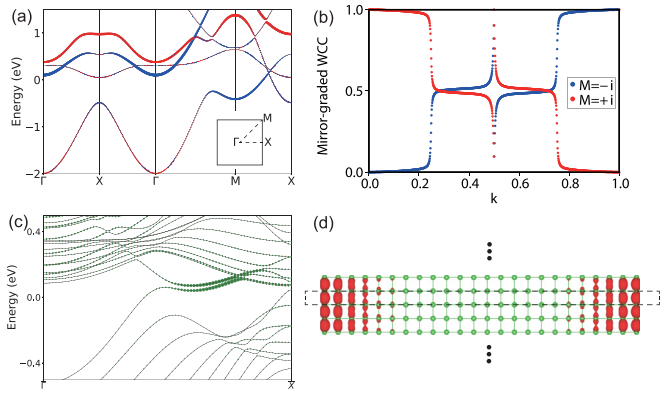

FIG. 5. (a) The orbital-resolved band structure of Ba monolayer. The red markers denote s, d_{z^2} orbitals and the blue markers denote $d_{x^2-y^2,xy}$ orbitals. The inset shows the high-symmetry **k** points in the first BZ. (b) Flow chart of the sum of the mirror-graded WCCs obtained by the Wilson-loop calculation for occupied bands with $\pm$ i mirror eigenvalues in the 2D BZ. (c) The band structure of the Ba nanoribbon where edge states are marked by green dots. (d) The partial charge density (red) of edge states in a nanoribbon of the Ba nanoribbon (green). The black dashed rectangle is the supercell used for first-principles calculations.

number is simply given by its winding number. As shown in Fig. 5(d), we find $\mathcal{C}_M = -2$ by tracing the evolution of the mirror-graded WCCs, consistent with the analysis from AMBI. Consequently, if we consider an open edge of the Ba monolayer, nontrivial helical edge states will appear. As shown in Fig. 5(b), topological edge states reside inside the gap, and merge to bulk around $\bar{X}$. The spatial charge distribution of edge states displayed in Fig. 5(c) confirms that they are localized at two edges. All these results consistently demonstrate that the Ba monolayer is indeed an AMBI-induced TCI.

E. Discussion

Before ending the section, we would like to discuss the band inversion in various TCI materials that are proposed previously. It is found that various TCI materials satisfy the AMBI mechanism, some of which even exhibit multiple AMBIs in the BZ, as listed in Table II. This implies the practicability of our proposed AMBI mechanism. For example, the cubic perovskite nitride $ThTaN_3$ is a TCI with the mirror Chern number of $\mathcal{C}_M = 2$ [89]. By analyzing the orbital components of bands near the Fermi level, we found that there are two AMBIs around the Γ point: one AMBI is between the Ta-d_{xy} and N-$p_{x,y}$ orbital and the other AMBI occurs between Ta-$d_{xz,yz}$ and N-p_z orbitals. As each AMBI contributes to a mirror Chern number of 1 according to Table I, the total mirror Chern number of $ThTaN_3$ is $\mathcal{C}_M = 2$, which agrees with the results from the first-principles calculation.

Another TCI material with multiple AMBIs is the famous SnTe class of IV-VI semiconductors [19,33,90,91]. Based on first-principles calculations, it is found that band inversions between the antibonding state (L_6^+ with even parity) of Te-$p_{x,y}$ and the bonding state (L_6^- with odd parity) of Sn-p_z orbitals occur at different L points in 3D bulk of SnTe. Similar band inversions also appear in X and Y points of 2D thin films of SnTe class of materials. Different from the simplified effective model discussed in Sec. II, the orbitals involved in the band inversion are from Sn and Te atoms, respectively. Therefore the inverted bonding and antibonding states have opposite parities but share the same mirror eigenvalues. Consequently, these band inversions belong to type-I and each AMBI contributes to the mirror Chern number by $|\Delta m_l| = 1$. By counting AMBIs in a 2D mirror plane of the BZ for 3D systems or in the entire BZ for 2D systems, we obtain the total mirror Chern number of $|\mathcal{C}_M| = 2$ for both 3D bulk [19] and 2D films [33,90] of the SnTe class of materials.

Lastly, we emphasize that although the mirror symmetry seems an important prerequisite for the analysis of AMBIs, the type-I AMBI mechanism can be generalized to analyze the band topology of materials without mirror symmetry. For instance, Zhang *et al.* [97] proposed the realization of the QSH state in a buckled honeycomb lattice via a band inversion between $p_{x,y}$ and p_z at Γ point. According to Table II, such a band inversion is of type-II, which would give rise to a TCI with $|\mathcal{C}_M| = 2$ if the mirror symmetry is preserved in the lattice. This discrepancy arises from the buckled structure

TABLE II. Overview of mirror protected TCI materials. The orbitals involved in AMBIs, the position of AMBI in the BZ, the mirror Chern number and the type of AMBI are listed.

material	orbitals	**k** point(s)	$\mathcal{C}_M$	type
$ThTaN_3$ [89]	Ta-d_{xy} vs N-$p_{x,y}$, Ta-$d_{xz,yz}$ vs N-p_z	Γ	2	I
SnTe [19]	Sn-p_z vs Te-$p_{x,y}$	L_1, L_2	−2	I
AB (*A* = Ge, Pb, Sn and *B* = S, Se, Te) monolayer [33,90]	A-p_z vs B-$p_{x,y}$	X, Y	−2	I
PbPo monolayer [91]	Pb-p_z vs Po-$p_{x,y}$	X, Y	2	I
Tl*M* (*M* = S and Se) (110) monolayer [36]	Tl-p_z vs S/Se-$p_{x,y}$	X, Y	−2	I
Na_3Bi monolayer [37]	Bi-s vs Bi-$p_{x,y}$	Γ	−1	I
OsC_{16} [92]	C-p_z vs Os-$d_{xz,yz}$	K	−1	I
HgTe/HgSe planar monolayer [93]	Hg-s vs Te/Se-$p_{x,y}$	Γ	1	I
NpSb monolayer [94]	Sb-$p_{x,y}$ vs Np-$d_{x^2-y^2}$	Γ	1	I
Na_2MnPb monolayer [95]	Mn-d_{z^2} vs Pb-$p_{x,y}$	Γ	1	I
Pt_3Sn (001) [96]	All-$p_{y,z}$ vs Pt-d_{yz}	Γ	−1	I
Pt_3Sn (1$\bar{1}$0) [96]	Pt-d_{xy} vs Pt-$d_{xz,yz}$	Γ	−2	II
Bi_3STe_2 [96]	Bi-p_z vs Bi-$p_{x,y}$	Γ	2	II
Ba monolayer [this work]	Ba-s, d_{z^2} vs Ba-$d_{x^2-y^2,xy}$	*M*	−2	I

which allows extra hopping terms that are forbidden in planar structures with the mirror symmetry. In the buckled honeycomb lattice without mirror symmetry, the mirror Chern number is no longer well defined, but the spin Chern number C_s is still determined by $|\Delta m_l| = 1$, indicating the topologically nontrivial QSH state.

V. CONCLUSION

In this paper, we discussed band inversions in terms of angular momenta for mirror protected topological states. We discussed in detail how the angular momentum of orbitals characterizing the band inversion influence the mirror Chern number $\mathcal{C}_M$ of TCIs. In particular, we showed that the mirror Chern number can be determined easily from the knowledge of the AMBI analysis for states at high-symmetry **k** points in the BZ. Using this method, we deduced that AMBI-induced topological states can be realized in various crystalline or disordered lattices based on model study and first-principles calculations.

There remain a number of further issues which need to be understood better. Although our work mainly focuses on nonmagnetic systems with time-reversal symmetry T, the AMBI is generally applicable to magnetic topological states, thus providing interesting future research directions. Beyond the mirror protected TCI phases, the similar AMBI analysis of topological states protected by other symmetry (such as the rotational, inversion and nonsymmorphic symmetry, or the combinations of time-reversal and spatial symmetries) is still ongoing. In addition, the recently discovered higher-order topological states, which stem from the double band inversion mechanism [98–101], may also be diagnosed by similar AMBI analysis. It will be of interest to provide a better understanding of these topological insulating and semimetallic states which are triggered by band inversion mechanisms.

ACKNOWLEDGMENTS

This work was supported by the National Natural Science Foundation of China (Grant No. 12074006), the National Key Research and Development Program of China (No. 2021YFA1401600), and the start-up fund from Peking University. The computational resources were supported by the high-performance computing platform of Peking University.

APPENDIX: DERIVATION OF EQ. (9)

Similar to the analysis of Eq. (6), one can expand $h(\mathbf{k})$ to the leading order of **k** near the Γ point,

$$h(\mathbf{k}) = \begin{pmatrix} \varepsilon_1' & \delta_1 k_-^{2m_1} & 0 & \lambda \\ \delta_1 k_+^{2m_1} & \varepsilon_1 & 0 & 0 \\ 0 & 0 & \varepsilon_2' & \delta_2 k_-^{-2m_1-2} \\ \lambda & 0 & \delta_2 k_+^{-2m_1-2} & \varepsilon_2 \end{pmatrix}, \quad \text{(A1)}$$

where λ is the spin-orbit coupling constant. Other entries in the nondiagonal block of Hamiltonian (A1) vanish for the conservation of spin angular momentum.

To obtain an effective model for the band inversion between $|m_1 + 1, m_1 + \frac{1}{2}\rangle$ and $|m_1, -m_1 + \frac{1}{2}\rangle$ orbitals, one can perform the analysis based on the standard perturbation theory, where the contributions from other states are treated as perturbations. This is reasonable since other bands are assumed to be far away from the inverted bands, and a small gap opened by λ is enough to ensure the topological property theoretically. Consequently, the reduced two-band effective Hamiltonian up to the first order of perturbation is

$$h_{\text{eff}}^{(0)}(\mathbf{k}) = \begin{pmatrix} \varepsilon_2 & 0 \\ 0 & \varepsilon_1 \end{pmatrix}.$$

According to the perturbation theory, the matrix element of the second order term reads

$$h_{aa'}^{(2)} = \frac{1}{2} \sum_b h'_{ab} h'_{ba'} \left(\frac{1}{\varepsilon_a - \varepsilon_b} + \frac{1}{\varepsilon_{a'} - \varepsilon_b} \right),$$

where h'_{ab} are elements in the Hamiltonian (A1). Here indices a and a' correspond to the reduced part and b corresponds to the perturbation part. Up to the leading order of **k** near Γ, the second order perturbation term of the reduced two-band effective Hamiltonian $h_{\text{eff}}(\mathbf{k})$ is

$$h_{\text{eff}}^{(2)}(\mathbf{k}) = \frac{1}{2} \left(\frac{1}{\varepsilon_2 - \varepsilon_1'} + \frac{1}{\varepsilon_1 - \varepsilon_1'} \right) \lambda \delta_1 (k_+^{\Delta m_j} \sigma_- + k_-^{\Delta m_j} \sigma_+),$$

where $\Delta m_j = (m_1 + 1/2) - (-m_1 + 1/2) = 2m_1$.

Finally, by neglecting an overall dispersion term which does not affect the band topology, one obtains the rescaled effective Hamiltonian

$$h_{\text{eff}}(\mathbf{k}) = \varepsilon \sigma_z + \lambda \delta (k_+^{\Delta m_j} \sigma_- + k_-^{\Delta m_j} \sigma_+).$$

[1] M. Z. Hasan and C. L. Kane, Colloquium: Topological insulators, Rev. Mod. Phys. **82**, 3045 (2010).
[2] X.-L. Qi and S.-C. Zhang, Topological insulators and superconductors, Rev. Mod. Phys. **83**, 1057 (2011).
[3] A. Bansil, H. Lin, and T. Das, Colloquium: Topological band theory, Rev. Mod. Phys. **88**, 021004 (2016).
[4] B. I. Halperin, Quantized Hall conductance, current-carrying edge states, and the existence of extended states in a two-dimensional disordered potential, Phys. Rev. B **25**, 2185 (1982).
[5] Y. Hatsugai, Chern Number and Edge States in the Integer Quantum Hall Effect, Phys. Rev. Lett. **71**, 3697 (1993).
[6] C. L. Kane and E. J. Mele, Quantum Spin Hall Effect in Graphene, Phys. Rev. Lett. **95**, 226801 (2005).
[7] C. L. Kane and E. J. Mele, Z_2 Topological Order and the Quantum Spin Hall Effect, Phys. Rev. Lett. **95**, 146802 (2005).
[8] B. A. Bernevig, T. L. Hughes, and S.-C. Zhang, Quantum spin hall effect and topological phase transition in HgTe quantum wells, Science **314**, 1757 (2006).
[9] H. Zhang, C.-X. Liu, X.-L. Qi, X. Dai, Z. Fang, and S.-C. Zhang, Topological insulators in Bi_2Se_3, Bi_2Te_3 and Sb_2Te_3 with a single Dirac cone on the surface, Nat. Phys. **5**, 438 (2009).
[10] L. Fu, Topological Crystalline Insulators, Phys. Rev. Lett. **106**, 106802 (2011).

[11] Y. Ando and L. Fu, Topological crystalline insulators and topological superconductors: From concepts to materials, Annu. Rev. Condens. Matter Phys. **6**, 361 (2015).

[12] C. Fang, M. J. Gilbert, and B. A. Bernevig, Bulk topological invariants in noninteracting point group symmetric insulators, Phys. Rev. B **86**, 115112 (2012).

[13] C. Fang, M. J. Gilbert, and B. A. Bernevig, Entanglement spectrum classification of C_n-invariant noninteracting topological insulators in two dimensions, Phys. Rev. B **87**, 035119 (2013).

[14] C.-K. Chiu, H. Yao, and S. Ryu, Classification of topological insulators and superconductors in the presence of reflection symmetry, Phys. Rev. B **88**, 075142 (2013).

[15] T. Morimoto and A. Furusaki, Topological classification with additional symmetries from Clifford algebras, Phys. Rev. B **88**, 125129 (2013).

[16] R.-J. Slager, A. Mesaros, V. Juričić, and J. Zaanen, The space group classification of topological band-insulators, Nat. Phys. **9**, 98 (2013).

[17] A. Alexandradinata, C. Fang, M. J. Gilbert, and B. A. Bernevig, Spin-Orbit-Free Topological Insulators without Time-Reversal Symmetry, Phys. Rev. Lett. **113**, 116403 (2014).

[18] K. Shiozaki and M. Sato, Topology of crystalline insulators and superconductors, Phys. Rev. B **90**, 165114 (2014).

[19] T. H. Hsieh, H. Lin, J. Liu, W. Duan, A. Bansil, and L. Fu, Topological crystalline insulators in the SnTe material class, Nat. Commun. **3**, 982 (2012).

[20] P. Dziawa, B. J. Kowalski, K. Dybko, R. Buczko, A. Szczerbakow, M. Szot, E. Łusakowska, T. Balasubramanian, B. M. Wojek, M. H. Berntsen, O. Tjernberg, and T. Story, Topological crystalline insulator states in $Pb_{1-x}Sn_xSe$, Nat. Mater. **11**, 1023 (2012).

[21] T. Liang, Q. Gibson, J. Xiong, M. Hirschberger, S. P. Koduvayur, R. J. Cava, and N. P. Ong, Evidence for massive bulk Dirac fermions in $Pb_{1-x}Sn_xSe$ from Nernst and thermopower experiments, Nat. Commun. **4**, 2696 (2013).

[22] Y. Okada, M. Serbyn, H. Lin, D. Walkup, W. Zhou, C. Dhital, M. Neupane, S. Xu, Y. J. Wang, R. Sankar, F. Chou, A. Bansil, M. Z. Hasan, S. D. Wilson, L. Fu, and V. Madhavan, Observation of dirac node formation and mass acquisition in a topological crystalline insulator, Science **341**, 1496 (2013).

[23] S.-Y. Xu, C. Liu, N. Alidoust, M. Neupane, D. Qian, I. Belopolski, J. D. Denlinger, Y. J. Wang, H. Lin, L. A. Wray, G. Landolt, B. Slomski, J. H. Dil, A. Marcinkova, E. Morosan, Q. Gibson, R. Sankar, F. C. Chou, R. J. Cava, A. Bansil *et al.*, Observation of a topological crystalline insulator phase and topological phase transition in $Pb_{1-x}Sn_xTe$, Nat. Commun. **3**, 1192 (2012).

[24] Y. Tanaka, T. Shoman, K. Nakayama, S. Souma, T. Sato, T. Takahashi, M. Novak, K. Segawa, and Y. Ando, Two types of Dirac-cone surface states on the (111) surface of the topological crystalline insulator SnTe, Phys. Rev. B **88**, 235126 (2013).

[25] M. Kargarian and G. A. Fiete, Topological Crystalline Insulators in Transition Metal Oxides, Phys. Rev. Lett. **110**, 156403 (2013).

[26] M. Kindermann, Topological Crystalline Insulator Phase in Graphene Multilayers, Phys. Rev. Lett. **114**, 226802 (2015).

[27] H. Weng, J. Zhao, Z. Wang, Z. Fang, and X. Dai, Topological Crystalline Kondo Insulator in Mixed Valence Ytterbium Borides, Phys. Rev. Lett. **112**, 016403 (2014).

[28] T. H. Hsieh, J. Liu, and L. Fu, Topological crystalline insulators and Dirac octets in antiperovskites, Phys. Rev. B **90**, 081112 (2014).

[29] T. Kawakami, T. Okamura, S. Kobayashi, and M. Sato, Topological Crystalline Materials of $J = 3/2$ Electrons: Antiperovskites, Dirac Points, and High Winding Topological Superconductivity, Phys. Rev. X **8**, 041026 (2018).

[30] Y. Kim, C. L. Kane, E. J. Mele, and A. M. Rappe, Layered Topological Crystalline Insulators, Phys. Rev. Lett. **115**, 086802 (2015).

[31] X. Li, F. Zhang, Q. Niu, and J. Feng, Superlattice valley engineering for designer topological insulators, Sci. Rep. **4**, 6397 (2014).

[32] J. Liu, T. H. Hsieh, P. Wei, W. Duan, J. Moodera, and L. Fu, Spin-filtered edge states with an electrically tunable gap in a two-dimensional topological crystalline insulator, Nat. Mater. **13**, 178 (2014).

[33] J. Liu, X. Qian, and L. Fu, Crystal field effect induced topological crystalline insulators in monolayer IV-VI semiconductors, Nano Lett. **15**, 2657 (2015).

[34] H. Ozawa, A. Yamakage, M. Sato, and Y. Tanaka, Topological phase transition in a topological crystalline insulator induced by finite-size effects, Phys. Rev. B **90**, 045309 (2014).

[35] E. O. Wrasse and T. M. Schmidt, Prediction of two-dimensional topological crystalline insulator in PbSe monolayer, Nano Lett. **14**, 5717 (2014).

[36] C. Niu, P. M. Buhl, G. Bihlmayer, D. Wortmann, S. Blügel, and Y. Mokrousov, Two-dimensional topological crystalline insulator and topological phase transition in TlSe and TlS monolayers, Nano Lett. **15**, 6071 (2015).

[37] C. Niu, P. M. Buhl, G. Bihlmayer, D. Wortmann, Y. Dai, S. Blügel, and Y. Mokrousov, Robust dual topological character with spin-valley polarization in a monolayer of the Dirac semimetal Na_3Bi, Phys. Rev. B **95**, 075404 (2017).

[38] C.-H. Hsu, Z.-Q. Huang, C. P. Crisostomo, L.-Z. Yao, F.-C. Chuang, Y.-T. Liu, B. Wang, C.-H. Hsu, C.-C. Lee, H. Lin, and A. Bansil, Two-dimensional topological crystalline insulator phase in Sb/Bi planar honeycomb with tunable dirac gap, Sci. Rep. **6**, 18993 (2016).

[39] C. M. Acosta and A. Fazzio, Spin-Polarization Control Driven by a Rashba-Type Effect Breaking the Mirror Symmetry in Two-Dimensional Dual Topological Insulators, Phys. Rev. Lett. **122**, 036401 (2019).

[40] J. C. Y. Teo, L. Fu, and C. L. Kane, Surface states and topological invariants in three-dimensional topological insulators: Application to $Bi_{1-x}Sb_x$, Phys. Rev. B **78**, 045426 (2008).

[41] T. Harman and I. Melngailis, in *Applied Solid State Science* (Elsevier, New York, 1974), Vol. 4, pp. 1–94.

[42] B. A. Volkov and O. A. Pankratov, Two-dimensional massless electrons in an inverted contact, JETP Lett. **42**, 178 (1985).

[43] O. Pankratov, S. Pakhomov, and B. Volkov, Supersymmetry in heterojunctions: Band-inverting contact on the basis of $Pb_{1-x}Sn_xTe$ and $Hg_{1-x}Cd_xTe$, Solid State Commun. **61**, 93 (1987).

[44] L. Fu and C. L. Kane, Topological insulators with inversion symmetry, Phys. Rev. B **76**, 045302 (2007).

[45] L. Fu, C. L. Kane, and E. J. Mele, Topological Insulators in Three Dimensions, Phys. Rev. Lett. **98**, 106803 (2007).

[46] H. Huang, Y. Xu, J. Wang, and W. Duan, Emerging topological states in quasi-two-dimensional materials, WIREs Comput. Mol. Sci. **7**, e1296 (2017).

[47] H. Huang, K.-H. Jin, and F. Liu, Alloy Engineering of Topological Semimetal Phase Transition in $MgTa_{2-x}Nb_xN_3$, Phys. Rev. Lett. **120**, 136403 (2018).

[48] H. Huang and F. Liu, Tensile strained gray tin: Dirac semimetal for observing negative magnetoresistance with Shubnikov-de Haas oscillations, Phys. Rev. B **95**, 201101 (2017).

[49] H. Huang, W. Jiang, K.-H. Jin, and F. Liu, Tunable topological semimetal states with ultraflat nodal rings in strained YN, Phys. Rev. B **98**, 045131 (2018).

[50] T. Zhang, Y. Jiang, Z. Song, H. Huang, Y. He, Z. Fang, H. Weng, and C. Fang, Catalogue of topological electronic materials, Nature (London) **566**, 475 (2019).

[51] F. Tang, H. C. Po, A. Vishwanath, and X. Wan, Comprehensive search for topological materials using symmetry indicators, Nature (London) **566**, 486 (2019).

[52] M. G. Vergniory, L. Elcoro, C. Felser, N. Regnault, B. A. Bernevig, and Z. Wang, A complete catalogue of high-quality topological materials, Nature (London) **566**, 480 (2019).

[53] T. L. Hughes, E. Prodan, and B. A. Bernevig, Inversion-symmetric topological insulators, Phys. Rev. B **83**, 245132 (2011).

[54] D. N. Sheng, Z. Y. Weng, L. Sheng, and F. D. M. Haldane, Quantum Spin-Hall Effect and Topologically Invariant Chern Numbers, Phys. Rev. Lett. **97**, 036808 (2006).

[55] T. Fukui and Y. Hatsugai, Topological aspects of the quantum spin-Hall effect in graphene: Z_2 topological order and spin Chern number, Phys. Rev. B **75**, 121403 (2007).

[56] E. Prodan, Robustness of the spin-Chern number, Phys. Rev. B **80**, 125327 (2009).

[57] H. Isobe and L. Fu, Theory of interacting topological crystalline insulators, Phys. Rev. B **92**, 081304 (2015).

[58] J. Liu, A short review on first-principles study of gapped topological materials, Comput. Mater. Sci. **195**, 110467 (2021).

[59] J. C. Slater and G. F. Koster, Simplified LCAO method for the periodic potential problem, Phys. Rev. **94**, 1498 (1954).

[60] S. Konschuh, M. Gmitra, and J. Fabian, Tight-binding theory of the spin-orbit coupling in graphene, Phys. Rev. B **82**, 245412 (2010).

[61] G. Kresse and J. Furthmüller, Efficiency of ab-initio total energy calculations for metals and semiconductors using a plane-wave basis set, Comput. Mater. Sci. **6**, 15 (1996).

[62] P. E. Blöchl, Projector augmented-wave method, Phys. Rev. B **50**, 17953 (1994).

[63] J. P. Perdew, K. Burke, and M. Ernzerhof, Generalized Gradient Approximation Made Simple, Phys. Rev. Lett. **77**, 3865 (1996).

[64] A. A. Mostofi, J. R. Yates, Y.-S. Lee, I. Souza, D. Vanderbilt, and N. Marzari, wannier90: A tool for obtaining maximally-localised Wannier functions, Comput. Phys. Commun. **178**, 685 (2008).

[65] Q. Wu, S. Zhang, H.-F. Song, M. Troyer, and A. A. Soluyanov, WannierTools: An open-source software package for novel topological materials, Comput. Phys. Commun. **224**, 405 (2018).

[66] T. Fukui, Y. Hatsugai, and H. Suzuki, Chern numbers in discretized brillouin zone: Efficient method of computing (spin) hall conductances, J. Phys. Soc. Jpn. **74**, 1674 (2005).

[67] A. A. Soluyanov and D. Vanderbilt, Computing topological invariants without inversion symmetry, Phys. Rev. B **83**, 235401 (2011).

[68] R. Yu, X. L. Qi, A. Bernevig, Z. Fang, and X. Dai, Equivalent expression of $\mathbb{Z}_2$ topological invariant for band insulators using the non-Abelian Berry connection, Phys. Rev. B **84**, 075119 (2011).

[69] S. T. Spees, J. R. Perumareddi, and A. W. Adamson, Crystal field energy levels for various symmetries, J. Phys. Chem. **72**, 1822 (1968).

[70] R. Penrose, The role of aesthetics in pure and applied mathematical research, Bull. Inst. Math. Appl. **10**, 266 (1974).

[71] H. Huang and F. Liu, Quantum Spin Hall Effect and Spin Bott Index in a Quasicrystal Lattice, Phys. Rev. Lett. **121**, 126401 (2018).

[72] H. Huang and F. Liu, Theory of spin Bott index for quantum spin Hall states in nonperiodic systems, Phys. Rev. B **98**, 125130 (2018).

[73] J. Fan and H. Huang, Topological states in quasicrystals, Front. Phys. **17**, 13203 (2022).

[74] H. Tsunetsugu, T. Fujiwara, K. Ueda, and T. Tokihiro, Eigenstates in 2-Dimensional Penrose Tiling, J. Phys. Soc. Jpn. **55**, 1420 (1986).

[75] O. Entin-Wohlman, M. Kléman, and A. Pavlovitch, Penrose tiling approximants, Journal de Physique **49**, 587 (1988).

[76] H. Tsunetsugu, T. Fujiwara, K. Ueda, and T. Tokihiro, Electronic properties of the Penrose lattice. I. Energy spectrum and wave functions, Phys. Rev. B **43**, 8879 (1991).

[77] H. Huang, Y.-S. Wu, and F. Liu, Aperiodic topological crystalline insulators, Phys. Rev. B **101**, 041103 (2020).

[78] H. Huang and F. Liu, A unified view of topological phase transition in band theory, Research **2020**, 7832610 (2020).

[79] X. Ni, H. Huang, and F. Liu, Robustness of topological insulating phase against vacancy, vacancy cluster, and grain boundary bulk defects, Phys. Rev. B **101**, 125114 (2020).

[80] C. Wang, T. Cheng, Z. Liu, F. Liu, and H. Huang, Structural Amorphization-Induced Topological Order, Phys. Rev. Lett. **128**, 056401 (2022).

[81] J. Li, Z. Zhang, C. Wang, H. Huang, B.-L. Gu, and W. Duan, Topological semimetals from the perspective of first-principles calculations, J. Appl. Phys. **128**, 191101 (2020).

[82] H. Huang, S. Zhou, and W. Duan, Type-II Dirac fermions in the $\mathbf{PtSe_2}$ class of transition metal dichalcogenides, Phys. Rev. B **94**, 121117 (2016).

[83] M. Yan, H. Huang, K. Zhang, E. Wang, W. Yao, K. Deng, G. Wan, H. Zhang, M. Arita, H. Yang, Z. Sun, H. Yao, Y. Wu, S. Fan, W. Duan, and S. Zhou, Lorentz-violating type-II Dirac fermions in transition metal dichalcogenide $PtTe_2$, Nat. Commun. **8**, 257 (2017).

[84] H. Huang, K.-H. Jin, and F. Liu, Black-hole horizon in the Dirac semimetal $Zn_2In_2S_5$, Phys. Rev. B **98**, 121110 (2018).

[85] B.-J. Yang and N. Nagaosa, Classification of stable three-dimensional Dirac semimetals with nontrivial topology, Nat. Commun. **5**, 4898 (2014).

[86] R. Li, H. Ma, X. Cheng, S. Wang, D. Li, Z. Zhang, Y. Li, and X.-Q. Chen, Dirac Node Lines in Pure Alkali Earth Metals, Phys. Rev. Lett. **117**, 096401 (2016).

[87] M. Hirayama, R. Okugawa, T. Miyake, and S. Murakami, Topological Dirac nodal lines and surface charges in fcc alkaline earth metals, Nat. Commun. **8**, 14022 (2017).

[88] H. Huang, J. Liu, D. Vanderbilt, and W. Duan, Topological nodal-line semimetals in alkaline-earth stannides, germanides, and silicides, Phys. Rev. B **93**, 201114 (2016).

[89] M.-C. Jung, K.-W. Lee, and W. E. Pickett, Perovskite $ThTaN_3$: A large-thermopower topological crystalline insulator, Phys. Rev. B **97**, 121104 (2018).

[90] Y.-z. Jia, W.-x. Ji, C.-w. Zhang, P. Li, S.-f. Zhang, P.-j. Wang, S.-s. Li, and S.-s. Yan, Prediction of topological crystalline insulators and topological phase transitions in two-dimensional PbTe films, Phys. Chem. Chem. Phys. **19**, 29647 (2017).

[91] Y.-P. Wang, W.-X. Ji, C.-W. Zhang, P. Li, and P.-J. Wang, A new topological crystalline insulator in two-dimensional PbPo with tunable large bulk gaps, J. Mater. Chem. C **4**, 8745 (2016).

[92] J. Zhou and P. Jena, Two-dimensional topological crystalline quantum spin Hall effect in transition metal intercalated compounds, Phys. Rev. B **95**, 081102 (2017).

[93] J. Li, C. He, L. Meng, H. Xiao, C. Tang, X. Wei, J. Kim, N. Kioussis, G. Malcolm Stocks, and J. Zhong, Two-dimensional topological insulators with tunable band gaps: Single-layer HgTe and HgSe, Sci. Rep. **5**, 14115 (2015).

[94] N. Mao, X. Hu, H. Wang, Y. Dai, B. Huang, Y. Mokrousov, and C. Niu, Magnetism-mediated transition between crystalline and higher-order topological phases in NpSb, Phys. Rev. B **103**, 195152 (2021).

[95] H. Wang, N. Mao, C. Niu, S. Shen, M.-H. Whangbo, B. Huang, and Y. Dai, Ferromagnetic dual topological insulator in a two-dimensional honeycomb lattice, Mater. Horiz. **7**, 2431 (2020).

[96] Z. Cao, F. Tang, D. Wang, and X. Wan, Systematic identification of mirror protected topological crystalline insulators by first-principles calculations, New J. Phys. **23**, 103032 (2021).

[97] H. Zhang, Y. Ning, W. Yang, R. Zhang, and X. Xu, Topological phase transition induced by $p_{x,y}$ and p_z band inversion in a honeycomb lattice, Nanoscale **11**, 13807 (2019).

[98] Z. Wang, B. J. Wieder, J. Li, B. Yan, and B. A. Bernevig, Higher-Order Topology, Monopole Nodal Lines, and the Origin of Large Fermi Arcs in Transition Metal Dichalcogenides XTe_2 ($X = \mathrm{Mo}, \mathrm{W}$), Phys. Rev. Lett. **123**, 186401 (2019).

[99] C.-H. Hsu, X. Zhou, T.-R. Chang, Q. Ma, N. Gedik, A. Bansil, S.-Y. Xu, H. Lin, and L. Fu, Topology on a new facet of bismuth, Proc. Natl. Acad. Sci. USA **116**, 13255 (2019).

[100] H. Huang, J. Fan, D. Li, and F. Liu, Generic orbital design of higher-order topological quasicrystalline insulators with odd five-fold rotation symmetry, Nano Lett. **21**, 7056 (2021).

[101] M. Pan, D. Li, J. Fan, and H. Huang, Two-dimensional Stiefel-Whitney insulators in liganded Xenes, npj Comput. Mater. **8**, 1 (2022).